Cryogenic MOS Transistor Model

Arnout Beckers, Farzan Jazaeri, and Christian Enz, *Senior Member, IEEE*

***Abstract*— This paper presents a physics-based analytical model for the MOS transistor operating continuously from room temperature down to liquid-helium temperature (4.2 K) from depletion to strong inversion and in the linear and saturation regimes. The model is developed relying on the 1-D Poisson equation and the drift-diffusion transport mechanism. The validity of the Maxwell–Boltzmann approximation is demonstrated in the limit to 0 K as a result of dopant freezeout in cryogenic equilibrium. Explicit MOS transistor expressions are then derived, including incomplete dopant ionization, bandgap widening, mobility reduction, and interface charge traps. The temperature dependence of the interface trapping process explains the discrepancy between the measured value of the subthreshold swing and the thermal limit at deep-cryogenic temperatures. The accuracy of the developed model is validated by experimental results on long devices of a commercial 28-nm bulk CMOS process. The proposed model provides the core expressions for the development of physically accurate compact models dedicated to low-temperature CMOS circuit simulation.**

***Index Terms*— Cryo-CMOS, cryogenic MOSFET, freeze-out, incomplete ionization, interface traps, low temperature, MOS transistor, physical modeling.**

I. Introduction

ADVANCED CMOS processes perform increasingly well from room temperature (RT) down to deep-cryogenic temperatures (<10 K) [1]–[3]. At these temperatures, the ideal switch with a steplike subthreshold slope comes within reach [4]. Furthermore, cryoelectronics [5]–[7] can provide an interface with superconducting devices on the quest for exascale supercomputing [8]. Ultimately, quantum-engineered devices controlled by cryo-CMOS circuits can bring new functionality to existing computing technologies [9], [10].

Large-scale integration of silicon spin qubits [11], [12] and cryo-CMOS control circuits is envisioned to take solid-state quantum computing to the next level [13]. Digital, analog, and RF CMOS circuits [14]–[16] are then required to operate at millikelvin temperatures for initialization, manipulation, and readout of the qubits, as well as error correction [17], [18]. Since the cooling power at millikelvin temperatures is reduced, the system could feature a cryogenic temperature gradient, where the control circuits operate at a higher cryogenic temperature than the qubits, e.g., at 4.2 K [14]. However, the optimal design of power-hungry and thermal-noise dissipating circuits operating in close proximity to the qubits is yet to be explored. In this context, the main hurdle to overcome is the lack of compact MOS transistor models in circuit simulators, remaining physically accurate below 10 K [14], [16].

Manuscript received March 21, 2018; revised May 21, 2018 and June 21, 2018; accepted July 4, 2018. Date of publication August 1, 2018; date of current version August 21, 2018. This work was supported by the European Union's Horizon 2020 Research & Innovation Programme under Grant Agreement 688539 MOS-Quito, MOS-based Quantum Information Technology, which aims to bring quantum computing to a CMOS platform. The review of this paper was arranged by Editor B. Iñiguez. *(Corresponding author: Arnout Beckers.)*

The authors are with the Integrated Circuits Laboratory, École Polytechnique Fédérale de Lausanne, 2000 Neuchâtel, Switzerland (e-mail: arnout.beckers@epfl.ch).

Color versions of one or more of the figures in this paper are available online at http://ieeexplore.ieee.org.

Digital Object Identifier 10.1109/TED.2018.2854701

II. Cryo-MOS Transistor Modeling

The low-temperature circuits developed for spacecraft [19], [20], scientific equipment [21], ultralow-noise detectors [22], cryobiology [23], and others have been custom-designed relying on a semiempirical approach. This approach requires laborious and expensive low-temperature measurements to extract model parameters for tuning RT compact models to the target low temperature [22], [24], [25]. Empirical temperature-scaling laws have been added to the RT physics-based MOS transistor model [26], [27] to capture cryogenic operation down to 4.2 K [28]–[30]. However, the discrepancy between the measured value of the subthreshold swing (SS) for a long device at 4.2 K (≈10 mV/decade) [3], [31], [32] and the theoretical thermal limit $U_T \ln 10$ (≈0.8 mV/decade) reveals that something more fundamental is missing. As we will demonstrate along this paper, important physical phenomena at low temperatures, such as interface trapping [27], [33] and incomplete ionization [34], [35], have not been properly included to date. Furthermore, the intrinsic carrier concentration, n_i, takes on extremely small values below 10 K, causing arithmetic underflow in implemented analytical expressions or convergence problems in computer-aided-design simulations [36]–[38]. Therefore, standard references on semiconductor devices treat only the cryogenic equilibrium condition in bulk semiconductors above 10 K [26], [27], [39]. Analytical device-physics models, starting from the Poisson equation at low temperature, leave a gap unfilled between the 0 K approximation and 77 K [40]–[43].

In this paper, we develop a MOS transistor model valid from RT down to deep-cryogenic temperatures, entirely based on physics principles and validated with experimental results. We start by verifying the continued validity of the Boltzmann statistics down to the deep-cryogenic regime.

III. MOS Electrostatics from RT to 4.2 K

We model a long, planar n-channel MOS field-effect transistor in silicon, as shown in Fig. 1. Uniform operation

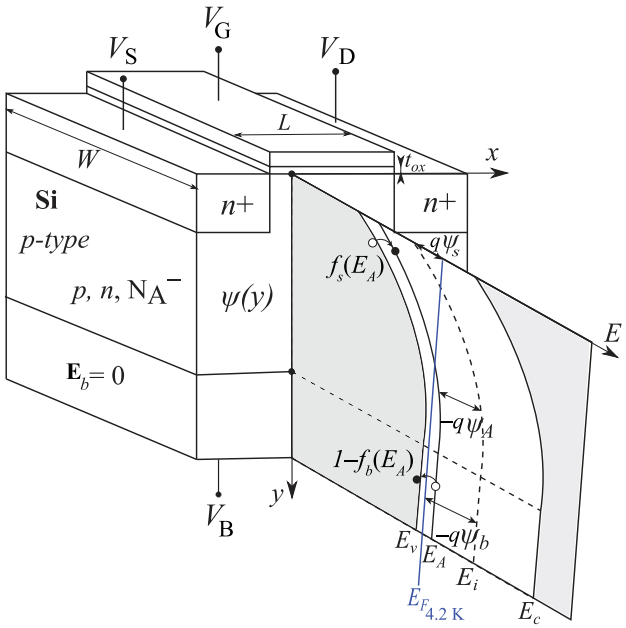

Fig. 1. Schematic of a long nMOS transistor with an annotated band diagram. The drift-diffusion and Poisson equations are solved along the *x*- and *y*-directions, respectively. At 4.2 K, and for doping concentrations ranging from 10^{12} to 10^{18} cm^{-3}, E_F lies below E_A in the bulk [see Fig. 2(a)], leading to bulk freezeout according to (2). When E_A bends under E_F near the surface, the acceptor dopants become rapidly completely ionized due to field-assisted ionization [i.e., the dopant-ionization probability near the surface, $f_s(E_A)$, is then close to one (see Fig. 4)]. The quasi-Fermi potential is not considered in this figure.

across the width of the transistor is assumed, and the gradual channel approximation is adopted. The electrostatics can then be described by the 1-D Poisson equation [26], [27].

A. Poisson–Fermi Equation

Merging the 1-D Poisson equation with the mobile carrier concentrations, n and p, given by Fermi–Dirac statistics, gives

$$\frac{\partial^2 \psi(y)}{\partial y^2} = -\frac{q}{\varepsilon_{si}}\left(-n + p - N_A^-\right) \tag{1}$$

where q is the elementary charge, ε_{si} is the silicon permittivity, and $\psi \triangleq (E_F - E_i)/q$ is the potential, with E_F the Fermi level and E_i the intrinsic energy level. The first term on the right-hand side (RHS) of (1) represents the electron contribution, n, the second term the hole contribution, p, and the third term the ionized dopant contribution, N_A^-.

1) Incompletely Ionized Dopants: Under thermal equilibrium, both at room and cryogenic temperatures, the majority carrier concentration can defer from the implanted doping value, N_A, due to incomplete ionization of the dopants. In cryogenic equilibrium, incomplete ionization is strong and known as freezeout, since thermal dopant ionization is very low [35]. However, during MOS operation, also field-assisted ionization comes into play. Fermi–Dirac statistics provides a fundamental way to model incomplete ionization which includes both dopant-ionization mechanisms. The concentration of ionized dopants, N_A^-, is then equal to the total concentration of implanted dopants times the Fermi–Dirac occupation probability of the acceptor energy E_A, i.e., $N_A \times f(E_A)$, or

$$N_A^- = \frac{N_A}{1 + g_A e^{\frac{E_A - E_{F,n}}{kT}}} = \frac{N_A}{1 + g_A e^{\frac{\psi_A - (\psi - V_{\text{ch}})}{U_T}}} \tag{2}$$

where the electron quasi-Fermi level is given by $E_{F,n} = E_F - qV_{\text{ch}}$. The RHS of (2) is obtained by replacing $E_A - E_{F,n}$ with $E_A - E_i + E_i - E_{F,n}$ in the exponential term and by defining an acceptor potential, $\psi_A \triangleq (E_A - E_i)/q$, as shown in Fig. 1. The channel voltage, V_{ch}, denotes the shift of the quasi-Fermi potential due to the drain-to-source voltage, V_{DS}. The second expression in (2) highlights the two dopant-ionization contributions, i.e., the potential (field-assisted ionization [35]) and temperature (thermal ionization). The acceptor-site degeneracy factor, g_A, is set to four due to fourfold degeneracy (heavy and light holes, spin up and down) [27], [39]. Note that setting g_A to zero is equivalent to assuming complete ionization.

2) Mobile Carrier Concentrations: Since n and p given by Fermi–Dirac statistics in (1) require numerical integration over energy, this inhibits explicit solutions for the charge densities and current in the MOS transistor. Expressing n and p using Boltzmann statistics allows to obtain such relations. However, the validity of the Maxwell–Boltzmann approximation down to deep-cryogenic temperatures is questionable. It has been reported [38], [42] that semiconductors become strongly degenerate at deep-cryogenic temperatures, preventing its use. This is, however, inconsistent with the 0 K limits of the Fermi-level position in the bandgap derived by Pierret and Neudeck [39]. Therefore, in Section III-A3, we aim to verify the Maxwell–Boltzmann approximation down to deep-cryogenic temperatures.

3) Verification of Boltzmann Statistics: We numerically calculate the position of the equilibrium Fermi level, E_F, down to 100 mK relying on the Fermi–Dirac statistics in an extrinsic bulk semiconductor, e.g., p-type silicon. In this case, the Poisson equation imposes the charge neutrality, $p_p = N_A^-$, where p_p is expressed by the Fermi–Dirac statistics [27], [39] and N_A^- by (2). This yields an implicit equation for E_F, which is solved numerically at each temperature and doping value using an extension of the arithmetic precision. As shown in Fig. 2(a), below 120 K, E_F remains off the valence-band edge with an offset larger than $3kT$ for doping values below the degenerate limit (i.e., $N_A = 4 \times 10^{18}$ cm^{-3} in Si:B) [27], [39], [45]. Note that this is predicted correctly only when incomplete ionization is considered. Complete ionization ($g_A = 0$) would predict an offset smaller than $3kT$ for $N_A = 10^{18}$ cm^{-3} and, hence, a degenerate semiconductor. It should, therefore, be emphasized that incomplete ionization maintains the nondegeneracy of a highly doped semiconductor at temperatures down to 100 mK. Furthermore, near 0 K, E_F tends to saturate at $(E_A - E_v)/2$ for all considered doping values. This corresponds to the 0 K limit by Pierret and Neudeck [39] assuming Boltzmann statistics. Using the now validated Maxwell–Boltzmann description for p_p, i.e., $N_v \exp[(E_v - E_F)/kT]$, in $p_p = N_A^-$, leads to a quadratic equation

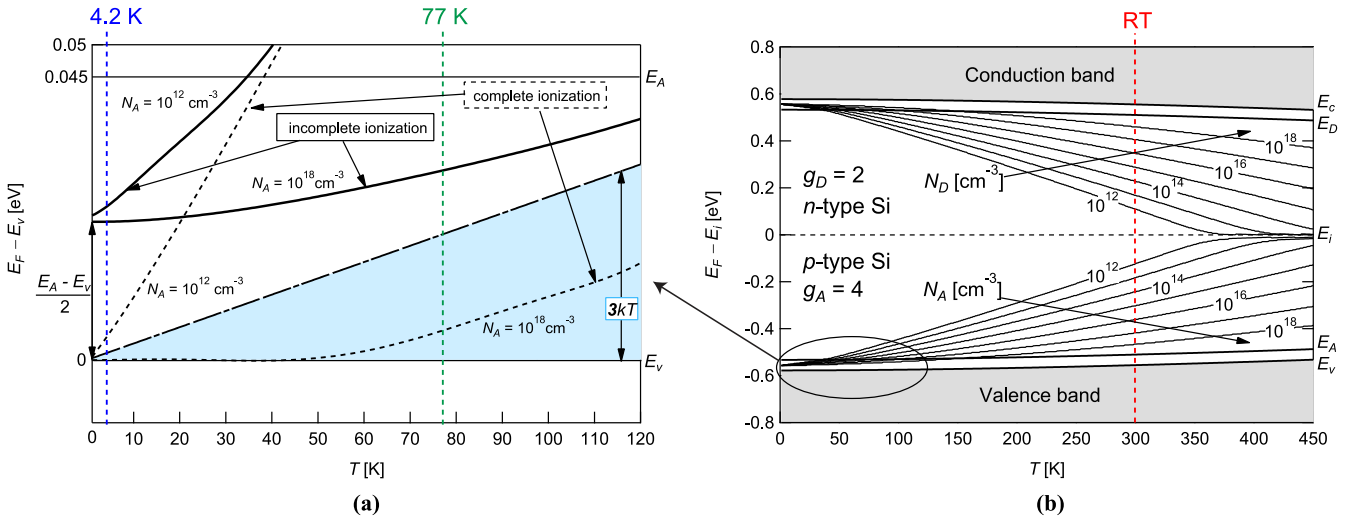

Fig. 2. Thermal equilibrium in extrinsic bulk silicon. (a) Magnified view of the cryogenic regime (below 120 K) in (b) for p-type Si. (b) Position of the Fermi level, E_F, in the bandgap as a function of doping and temperature. The E_F-position is calculated from RT down to 100 mK using an extension of the arithmetic precision and an E_F-resolution of 1 meV. When incomplete ionization is considered, the distance of E_F to the valence-band edge, E_V, stays larger than $3kT$, validating the use of the Maxwell–Boltzmann approximation down to millikelvin temperatures. This figure applies to the bulk of the MOS transistor in all regions of operation and to the whole body of the MOS transistor in the flat-band condition. Bandgap temperature dependence is taken by Varshni [44] and a standard, temperature-independent value of $E_A - E_V = 0.045$ eV in Si:B is assumed.

in $\exp[(E_v - E_F)/kT]$ with as solution

$$E_F - E_v = kT \ln \frac{N_v}{N_A} + kT \ln \frac{1 + \sqrt{1 + 4 g_A \frac{N_A}{N_v} e^{\frac{E_A - E_v}{kT}}}}{2}. \quad (3)$$

Considering the temperature dependence of N_v [27], [39], while taking the limit of (3) to 0 K, leads to $\lim_{T \to 0\ K} E_F = E_v + (E_A - E_v)/2$.

Performing the same numerical E_F-calculation for an intrinsic semiconductor, the extremely small value of n_i can be verified relying on the Fermi–Dirac statistics. The Poisson equation then imposes the charge neutrality, $n = p = n_i$, where n and p are given by the Fermi–Dirac statistics. As shown in Fig. 3, this yields n_i values lying outside the range of the IEEE double-precision arithmetic (10^{-308} – 10^{308}), e.g., at 4.2 K, $n_i \approx 10^{-678}$ cm^{-3}. Therefore, an extension of the arithmetic precision will also be used in the remainder of this paper based on the Boltzmann statistics, since the carrier concentrations are then expressed through n_i.

B. Poisson–Boltzmann Equation

Using the Maxwell–Boltzmann approximation of n and p, validated down to deep-cryogenic temperatures in Section III-A3, we combine the 1-D Poisson equation with the Boltzmann statistics, which leads to

$$\frac{\partial^2 \psi(y)}{\partial y^2} = -\frac{q}{\varepsilon_{si}} \left(-n_i e^{\frac{\psi - V_{ch}}{U_T}} + n_i e^{-\frac{\psi}{U_T}} - N_A^- \right) \quad (4)$$

where $U_T \triangleq kT/q$ is the thermal voltage. The first term on the RHS of (4) represents the electron contribution, n, and the second term the hole contribution, p. The intrinsic carrier concentration is given by $n_i = \sqrt{N_c N_v} \exp(-E_g/2kT)$, where E_g is the bandgap and N_c and N_v are the effective density of states in the conduction and valence bands, respectively. The temperature dependence of E_g as described by Varshni [44] is used. The extremely small, but a finite value of n_i at deep-cryogenic temperatures cannot be assumed 0—which would

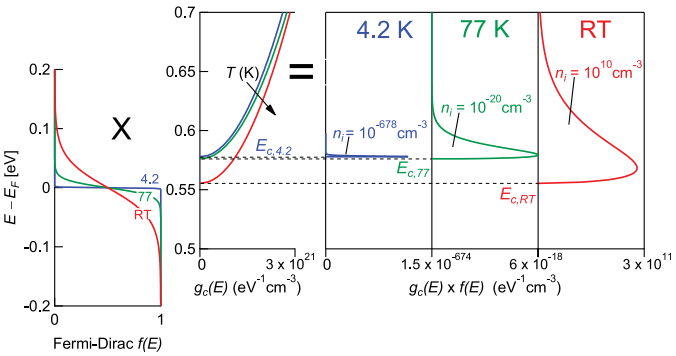

Fig. 3. Intrinsic carrier concentration reaches extremely small values at 4.2 K. Left: Fermi–Dirac distribution function approaching a step function at 4.2 K. Middle: density of states in the conduction band. Right: overlap between the density of states in the conduction band and the Fermi–Dirac distribution function at 4.2 K, 77 K, and RT. The overlap function $g_c(E) \times f(E)$ becomes extremely small in magnitude and very peaked at 4.2 K. The area under the overlap function is equal to the intrinsic carrier concentration. Bandgap temperature dependence used by Varshni [44] and effective mass values by Pierret and Neudeck [39].

be equivalent to the 0 K approximation [40] or considering $f(E)$ as a step function—since this leads to zero mobile carrier concentrations independently of the potential. This is irreconcilable with the observed field-effect and correct functioning of the MOS transistor at 4.2 K [4], [31]. For smaller U_T, the exponential factor has a very big dynamic range when ψ changes during the MOS transistor operation, large enough to overrule n_i in the multiplication.

1) Derivation of the Electric Field at the Surface: Introducing (2) for N_A^- in (4) and then multiplying (4) on both sides with $2(\partial\psi/\partial y)$ give

$$\frac{\partial}{\partial y} \left[\left(\frac{\partial \psi(y)}{\partial y} \right)^2 \right] = \frac{2q}{\varepsilon_{si}} \left(n_i e^{\frac{\psi - V_{ch}}{U_T}} - n_i e^{-\frac{\psi}{U_T}} + \frac{N_A}{1 + g_A e^{\frac{\psi_A - (\psi - V_{ch})}{U_T}}} \right) \frac{\partial \psi}{\partial y}. \quad (5)$$

Integrating (5) from bulk to surface with $\mathbf{E} = -\partial\psi/\partial y$ and $\mathbf{E}_b = 0$ yields

$$\mathbf{E}_s^2 = \frac{2q}{\varepsilon_{si}} \int_{\psi_b}^{\psi_s} \left(n_i e^{\frac{\psi - V_{\text{ch}}}{U_T}} - n_i e^{-\frac{\psi}{U_T}} + \frac{N_A}{1 + g_A e^{\frac{\psi_A - (\psi - V_{\text{ch}})}{U_T}}} \right) d\psi. \tag{6}$$

In (6), the additional potential dependence due to field-assisted ionization of the dopants can be straightforwardly integrated as well, i.e., by replacing N_A with $N_A\{1 + g_A \exp[(\psi_A - (\psi - V_{\text{ch}}))/U_T] - g_A \exp[(\psi_A - (\psi - V_{\text{ch}}))/U_T]\}$ in the numerator of the third term and splitting the resulting integral. This gives an expression for the square of the electric field at the surface

$$\mathbf{E}_s^2 = \frac{2qn_iU_T}{\varepsilon_{si}} \left(e^{\frac{\psi_s - V_{\text{ch}}}{U_T}} - e^{\frac{\psi_b - V_{\text{ch}}}{U_T}} + e^{-\frac{\psi_s}{U_T}} - e^{-\frac{\psi_b}{U_T}} \right) + \frac{2qN_A}{\varepsilon_{si}} \left[\psi_s - \psi_b - U_T \ln \frac{f_s(E_A)}{f_b(E_A)} \right] \tag{7}$$

where $\psi_b \triangleq (E_{F,b} - E_i)/q$ is the bulk potential and $\psi_s \triangleq (E_{F,s} - E_i)/q$ is the surface potential, as indicated in Fig. 1. $E_{F,s}$ denotes the Fermi level at the surface, and $E_{F,b}$ denotes the Fermi level in the bulk. The logarithmic term in (7) is the contribution of incomplete ionization, where

$$f_s(E_A) \triangleq \frac{1}{1 + g_A e^{\frac{E_A - E_{F,s}}{kT}}} = \frac{1}{1 + g_A e^{\frac{\psi_A - (\psi_s - V_{\text{ch}})}{U_T}}} \tag{8}$$

is the Fermi–Dirac ionization probability at the surface, and

$$f_b(E_A) \triangleq \frac{1}{1 + g_A e^{\frac{E_A - E_{F,b}}{kT}}} = \frac{1}{1 + g_A e^{\frac{\psi_A - \psi_b}{U_T}}} \tag{9}$$

the Fermi–Dirac ionization probability in the bulk, assuming that V_{ch} is zero in the bulk. Both ionization probabilities are qualitatively shown in Fig. 1. If complete ionization is assumed, then $f_s(E_A) = f_b(E_A) = 1$ and the incomplete ionization term cancels in (7), leading to the expression widely used at RT [26], [27]. The surface-ionization probability $f_s(E_A)$ is shown in Fig. 4 as a function of thermal and field-assisted ionization. Immediately evident is that freezeout at the surface (arbitrarily defined when $f_s(E_A) < 0.2$) is only present when the temperature is below ≈50 K and the potential is close to the flat-band condition ($\psi_s \approx \psi_b$). Above ψ_b, the ionization probability rapidly transitions to one due to field-assisted ionization. This transition corresponds to the bending of E_A under E_F at the surface in Fig. 1. Therefore, complete ionization is a valid approximation even at deep-cryogenic temperatures, although the shift in E_F due to incomplete ionization [Fig. 2(a)] should be considered since it affects the threshold voltage. This E_F-shift can be quantified by using $f_b(E_A)$ from (9) in the bulk charge neutrality condition, $p_p = N_A^-$, which leads to the quadratic equation $\exp(2\psi_b/U_T) - (n_i/N_A)\exp(\psi_b/U_T) - (g_A/N_A)\exp(\psi_A/U_T)$ with the solution

$$\psi_b = U_T \ln \frac{n_i}{N_A} + U_T \ln \frac{1 + \sqrt{1 + 4g_A \frac{N_A}{n_i} e^{\frac{\psi_A}{U_T}}}}{2}. \tag{10}$$

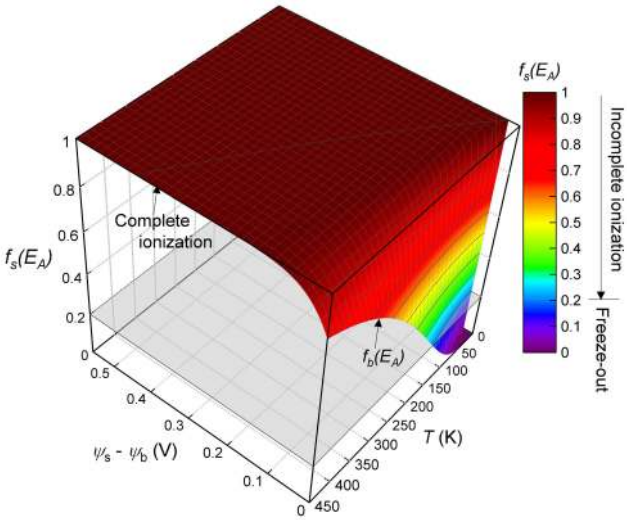

Fig. 4. Dopant ionization at the surface is an interplay between the thermal ionization (T) and the field-assisted ionization ($\psi_s - \psi_b$). Freezeout is assumed when 20% of the dopants are ionized. This happens only when T is below ≈50 K and close to the flat-band condition ($\psi_s \approx \psi_b$). When ψ_s increases, a rapid transition takes place to complete ionization for all temperatures. In the flat-band condition ($\psi_s = \psi_b$), the ionization probability at the surface is only due to thermal ionization and equals the ionization probability in the bulk, $f_b(E_A)$.

The second term in (10) is the shift of E_F by including incomplete ionization, which is only dependent on temperature and doping. Assuming complete ionization, i.e., $g_A = 0$, the well-known $U_T \ln(n_i/N_A)$ is obtained.

2) Derivation of the Charge Densities: Applying the Gauss law over the semiconductor body, the total semiconductor charge density per unit area, Q_{sc}, is obtained by $Q_{sc} = -\varepsilon_{si}\mathbf{E}_s$, with $\mathbf{E}_s$ given by (7). The obtained Q_{sc} is shown in Fig. 5(a) at RT, 77 K, and 4.2 K. For 77 and 4.2 K, small kinks are noticeable close to ψ_b due to the transition from incomplete to complete ionization when E_A bends under E_F at the surface ($E_{F,s}$), or equivalently, ψ_s becomes less negative than ψ_A. Above this transition, $f_s(E_A) \approx 1$ according to (2). At RT, E_F lies above E_A in the flat-band condition [see Fig. 2(b)], and hence, no transitional kink is noticeable. There is, however, a ψ_b-shift also at RT due to incomplete ionization according to (10). Note that for complete ionization (dashed lines), no kinks are observed since the logarithmic term cancels in (7). Assuming the charge-sheet and fully depletion approximations [26], the fixed charge density per unit area, Q_f, is given by

$$Q_f = -\varepsilon_{si} \sqrt{\frac{2qN_A}{\varepsilon_{si}}(\psi_s - \psi_b) - \frac{2qN_AU_T}{\varepsilon_{si}} \ln \frac{f_s(E_A)}{f_b(E_A)}}. \tag{11}$$

Relying on the charge neutrality, the mobile charge density per unit area, Q_m, can be obtained from $Q_m = Q_{sc} - Q_f$, resulting in (12), as shown at the bottom of the next page. Q_m is shown in Fig. 6(a) for RT, 77 K, and 4.2 K. As can be observed in Fig. 6(a), incomplete ionization does not affect the turn-ON rate of Q_m, but it contributes a small decrease in the charge-threshold voltage. The latter is due to E_F lying closer to the conduction band when including

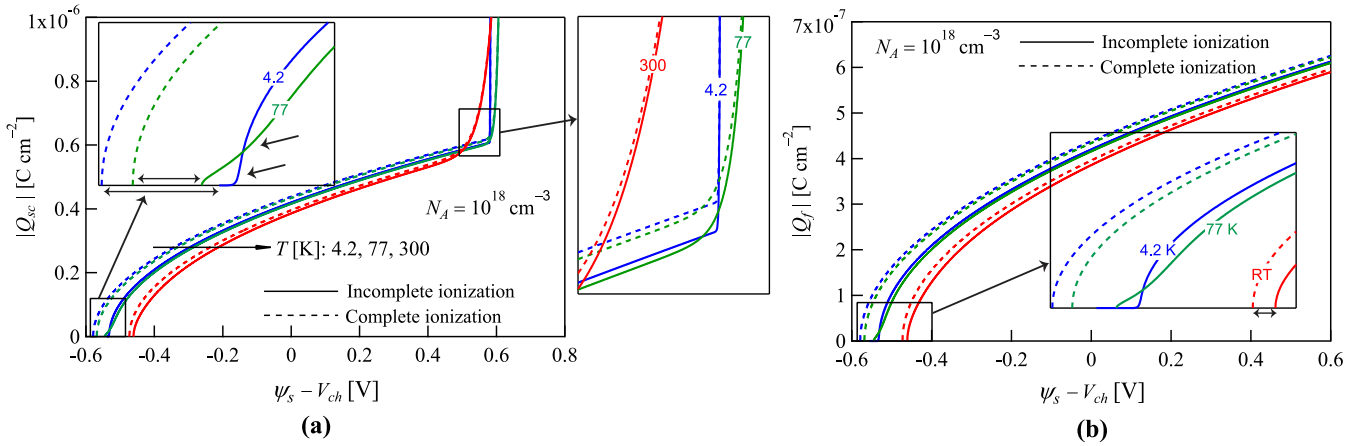

Fig. 5. (a) Total semiconductor charge density, Q_{sc}, and (b) fixed charge density, Q_f, at RT (red lines), liquid-nitrogen temperature (77 K, green lines), and liquid-helium temperature (4.2 K, blue lines) including incomplete ionization (solid lines) or assuming complete ionization (dashed lines). The potential is swept starting from the bulk potential, ψ_b, calculated at a given temperature and doping according to (10). Horizontal arrows show the shifts in ψ_b by including incomplete ionization at a given temperature. Skewed arrows in the insets indicate the kinks at 77 and 4.2 K due to the transition from incomplete to complete ionization when E_A bends under E_F (Fig. 1).

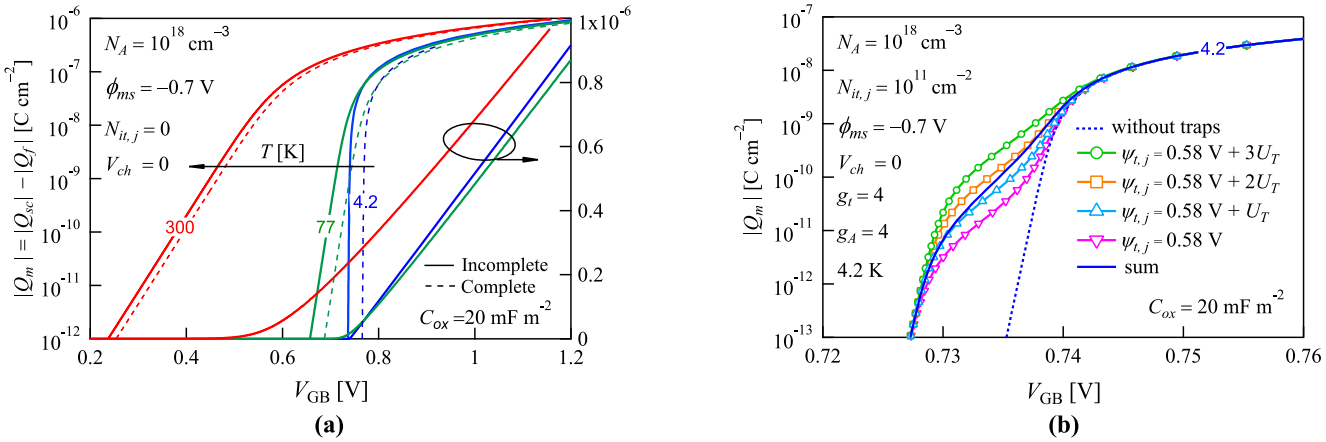

Fig. 6. (a) Mobile charge density, Q_m, without interface traps at RT, 77 K, and 4.2 K including incomplete ionization (solid lines), and assuming complete ionization (dashed lines). Incomplete ionization yields a small decrease in the charge-threshold voltage. (b) Influence of four single interface traps close to the conduction band, and their combined effect on the turn-ON rate of Q_m at 4.2 K.

incomplete ionization, as shown in Fig. 2(a) and derived in (10).

Therefore, from this section, we conclude that incomplete ionization cannot explain the offset between the measured SS at 4.2 K and the thermal limit. As we will show in Section III-B3, the temperature-dependent occupation of interface charge traps can degrade the SS down to 4.2 K.

3) Interface Charge Traps: Defects and lattice breaking at the oxide–semiconductor interface introduce the trap energy levels, E_t, in the bandgap which degrade the control of the gate-to-bulk voltage, V_{GB}, over the channel. In what follows, the Fermi–Dirac occupation of interface traps, $f(E_t)$, is included in the surface-boundary condition and the effect on the Q_m turn-ON rate is analyzed at 4.2 K. The surface-boundary condition, i.e., the link between V_{GB} and ψ_s, is given by $V_{GB} = V_{FB} + \varepsilon_{si}\mathbf{E}_s/C_{ox} + (\psi_s - \psi_b)$, where C_{ox} is the oxide capacitance per unit area and V_{FB} is the flat-band voltage, given by $V_{FB} \triangleq \phi_{ms} - Q_{it}/C_{ox}$ [26], [27]. Here, Q_{it} is the interface-trap charge density per unit area. We consider a summation of discrete acceptor trap energy levels [46] (all donor states are occupied and neutral during turn ON in nMOS [27]). Each discrete trap energy level, $E_{t,j}$, at position j in the bandgap has its particular $N_{it,j}$-value assigned to it, where N_{it} is the density-of-interface traps per unit area. Q_{it} can then be expressed as $Q_{it} = -q\sum_j^N N_{it,j} f_s(E_{t,j})$, where N is the number of interface traps, and

$$f_s(E_{t,j}) = \frac{1}{1 + g_t e^{\frac{E_{t,j} - E_{F,s}}{kT}}} = \frac{1}{1 + g_t e^{\frac{\psi_{t,j} - (\psi_s - V_{ch})}{U_T}}} \tag{13}$$

$$Q_m = -\varepsilon_{si}\sqrt{\frac{2qn_iU_T}{\varepsilon_{si}}\left(e^{\frac{\psi_s - V_{ch}}{U_T}} - e^{\frac{\psi_b - V_{ch}}{U_T}}\right) + \frac{2qN_A}{\varepsilon_{si}}\left[\psi_s - \psi_b - U_T \ln\frac{f_s(E_A)}{f_b(E_A)}\right]} + \varepsilon_{si}\sqrt{\frac{2qN_A}{\varepsilon_{si}}\left[(\psi_s - \psi_b) - U_T \ln\frac{f_s(E_A)}{f_b(E_A)}\right]} \tag{12}$$

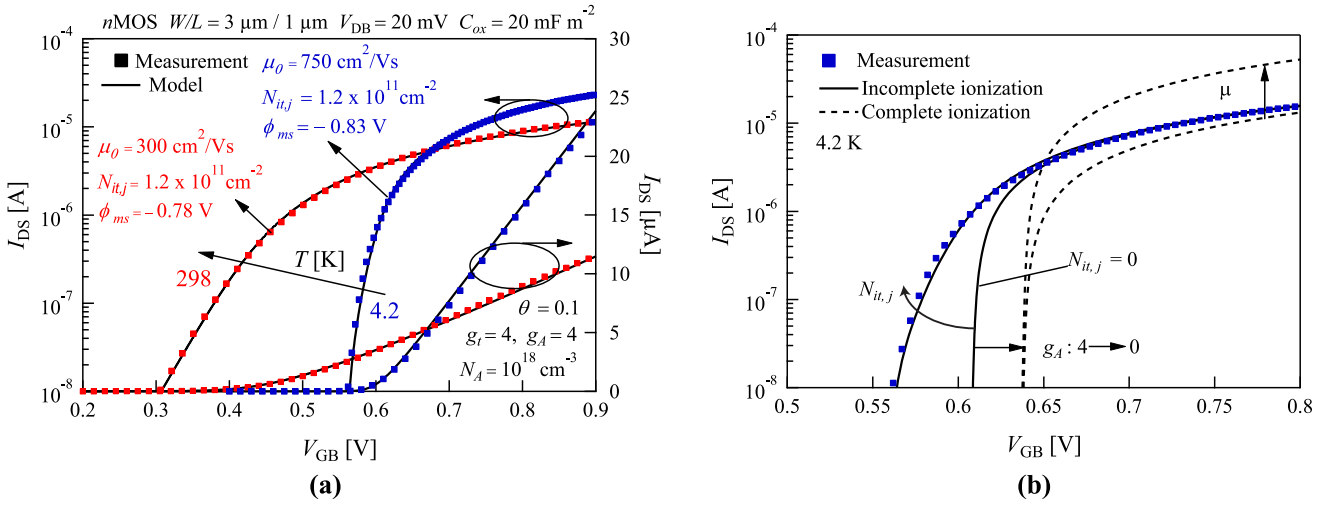

Fig. 7. (a) Linear model validation with measurements at RT and 4.2 K on a long nMOS device (a 28-nm bulk CMOS process). In the measurements, the gate voltage was swept from 0.2 to 0.9 V with a step size of 1 mV in order to reliably resolve the steep subthreshold slope at cryogenic temperature. The sets of physical model parameters are shown for each temperature. Five interface traps are placed at $\psi_{t,j} = 0.58\ \text{V} - 2U_T : U_T : 0.58\ \text{V} + 2U_T$. (b) Overview of the phenomena influencing the current at 4.2 K: incomplete ionization ($g_A = 4$) leads to a decrease in the threshold voltage; interface traps ($N_{it,j}$) strongly degrade the subthreshold slope, and mobility (μ) increases the ON-state current.

is the Fermi–Dirac occupation probability of the trap energy level $E_{t,j}$. The RHS of (13) is obtained by defining the trap potentials, $\psi_{t,j} \triangleq (E_{t,j} - E_i)/q$ [46]–[48]. This leads to the flat-band voltage

$$V_{\text{FB}} = \phi_{ms} + \frac{q}{C_{\text{ox}}} \sum_{j}^{N} \frac{N_{\text{it},j}}{1 + g_t \exp\{[\psi_{t,j} - (\psi_s - V_{\text{ch}})]/U_T\}}. \tag{14}$$

Plotting Q_m from (12) versus V_{GB} at 4.2 K in Fig. 6(b), including four interface traps close to the conduction band, reveals how each interface trap degrades the turn ON of Q_m separately, as well as the combined effect of the sum of the interface traps.

IV. Current Derivation

To derive the current in the linear regime, this core model assumes drift-diffusion transport and does not include ballistic nor quantum transport. To verify the drift-diffusion transport mechanism at cryogenic temperatures, the proposed model for the drain-to-source current will be experimentally validated in Section V. Neglecting the hole contribution to the current, the expression for the total drain–source current is given by $I_{\text{DS}} = -\mu_n (W/L) \int_{V_{\text{SB}}}^{V_{\text{DB}}} Q_m(V_{\text{ch}}) dV_{\text{ch}}$, where the electron mobility μ_n is assumed constant along the channel and W/L is the device aspect ratio, as shown in Fig. 1. In the linear regime, Q_m can be assumed independent of V_{ch}. In this case, the total drain–source current is given by $I_{\text{DS}} = -\mu_n (W/L) Q_m V_{\text{DS}}$. In saturation, the integral over V_{ch} cannot be readily solved. Therefore, starting from the drift-diffusion equation gives

$$I_{\text{DS}} = -\frac{W}{L} \int_{\psi_{s,S}}^{\psi_{s,D}} \mu_n Q_m d\psi + \frac{W}{L} \int_{Q_{m,S}}^{Q_{m,D}} \mu_n U_T dQ_m. \tag{15}$$

Assuming a linearization of the mobile charge density with respect to the surface potential at constant gate voltage [49] in (15), i.e., $Q_m = mC_{\text{ox}}(\psi_s - \psi_P)$, with $m \triangleq \partial(Q_m/C_{\text{ox}})/\partial\psi_s$ and ψ_P the pinchoff potential, and integrating, results in an expression for the total drain–source current in saturation

$$I_{\text{DS}} = \frac{W}{L} \mu_n \left[-\frac{Q_{m,D}^2 - Q_{m,S}^2}{2mC_{\text{ox}}} + U_T (Q_{m,D} - Q_{m,S}) \right]. \tag{16}$$

$Q_{m,S}$ and $Q_{m,D}$ are obtained from (12), setting V_{ch} to zero and V_{DS}, respectively. At cryogenic temperature, an improvement in the low-field mobility, μ_0, is observed due to a reduction of the phonon scattering [1], [5]. In addition, the mobility reduces at higher gate voltages due to the surface-roughness scattering associated with high vertical electric field [1]. This mobility reduction can be modeled by $\mu_n = \mu_0/(1 + \theta V_{\text{GB}})$, where θ is the mobility-reduction factor [50]. It should be highlighted that the developed model is a core model for long devices. Short-channel effects, impact ionization, self-heating, and hot-carrier degradation should obviously be included in a fully predictive model after the validation of the long-channel model at cryogenic temperatures.

V. Experimental Results and Discussion

RT and cryogenic measurements were performed on devices fabricated in a 28-nm bulk CMOS process. The full set of measurements, measurement setup, and characterization were previously reported in [3] and [31]. After measuring at RT, the samples were immersed into liquid helium (4.2 K) and liquid nitrogen (77 K) baths with a dipstick. Fig. 7(a) favorably compares the model with the linear transfer characteristics ($V_{\text{DB}} = 20$ mV) measured at RT and 4.2 K on a long nMOS device with $W/L = 3$ µm/1 µm in the linear and logarithmic scales. The extracted μ_0 values from the model are in accordance with the characterization performed in [31]. Furthermore, Fig. 7(b) analyzes the effect of incomplete ionization, interface traps, and mobility on the current at 4.2 K. Note that incomplete ionization reduces the threshold voltage, and interface traps can degrade the SS to ≈10 mV/decade.

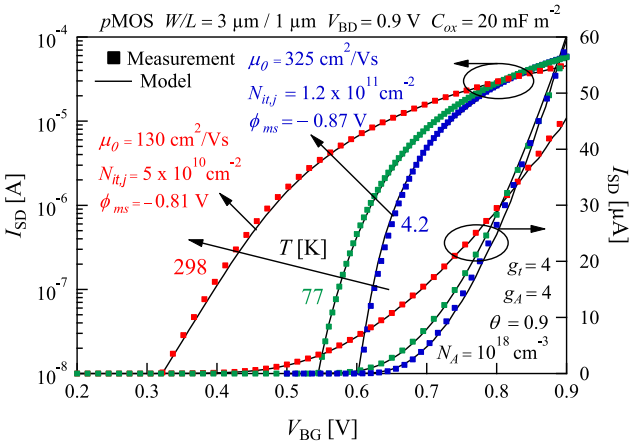

Fig. 8. Saturation model validation with measurements at RT, 77 K, and 4.2 K on a long pMOS device (a 28-nm bulk CMOS process). Four interface traps are placed at $\psi_{t,j} = 0.58\ \text{V} - 2U_T : U_T : 0.58\ \text{V} + U_T$. The used physical model parameters for RT and 4.2 K are shown in the figure. For 77 K, the model parameters are $\phi_{ms} = -0.87$ V, $N_{it,j} = 1.1 \times 10^{11}\ \text{cm}^{-2}$, and $\mu_0 = 300\ \text{cm}^2\ \text{V}^{-1}\text{s}^{-1}$.

The strong increase in the mobility increases the ON-state current at 4.2 K. Fig. 8 validates the model for the current in saturation ($|V_{DB}| = 0.9$ V) using the measurements performed at RT, 77 K, and 4.2 K on a long pMOS device with $W/L = 3\ \mu\text{m}/1\ \mu\text{m}$ in the linear and logarithmic scales. The metal–semiconductor work function difference, ϕ_{ms}, increases in an absolute value at lower temperatures according to the change in E_F-position (Fig. 2).

VI. Subthreshold-Swing Derivation

In this section, an expression for the SS, including incomplete ionization and temperature-dependent interface trapping, is derived. Incomplete ionization is included to prove the minimal influence on SS, as shown in Fig. 7(b). The temperature dependence of interface-trap occupation, $f_s(E_t)$, allows to obtain the Δ_{SS}-offset of ≈10 mV/decade above the thermal limit, $U_T \ln 10$, previously observed on long devices [3], [31].

The SS is usually expressed as $nU_T \ln 10$, where the non-ideality factor or slope factor, n, is given by $(\partial V_{GB}/\partial\psi_s)$, describing the deviation from the thermal limit. Assuming $f_s(E_t)$ from (13) to be one, $(\partial V_{GB}/\partial\psi_s)$ yields $1 + (2qN_A\varepsilon_{si})^{1/2}/[C_{ox}(2\sqrt{\psi_s - \psi_b})] + qN_{it}/C_{ox}$ [26], [51]. However, at 4.2 K, and assuming the highest possible doping value below the degenerate limit, a large N_{it} value in the order of $10^{13}\ \text{cm}^{-2}$ is extracted to accommodate for an SS of ≈10 mV/decade [33], [52], since N_{it} becomes multiplied with U_T in this expression. However, it should be emphasized that in the used expression for SS, the temperature dependence of interface-trap occupation is not considered. Relying on drift-diffusion transport in the linear regime and assuming μ independent of V_{GB}, the subthreshold slope, SS^{-1}, is given by

$$\text{SS}^{-1} = \frac{1}{\ln 10}\frac{1}{Q_m}\frac{\partial Q_m}{\partial\psi_s}\frac{\partial\psi_s}{\partial V_{GB}}. \tag{17}$$

The factor $(1/Q_m)(\partial Q_m/\partial\psi_s)$ is found from (12) by considering $Q_m \ll Q_f$ or $Q_{sc} \approx Q_f$ in the subthreshold region. After some mathematical manipulation, we find

$$\frac{1}{Q_m}\frac{\partial Q_m}{\partial\psi_s} = q\varepsilon_{si}\left[\frac{1}{Q_m Q_f}n_i e^{\frac{\psi_s - V_{ch}}{U_T}} - \frac{1}{Q_f^2}N_A\left(1 - \frac{U_T}{f_s(E_A)}\frac{\partial f_s(E_A)}{\partial\psi_s}\right)\right]. \tag{18}$$

Merging (11), (17), and (18) and inverting give

$$\text{SS} = \frac{2N_A \ln 10\left[(\psi_s - \psi_b) - U_T \ln\frac{f_s(E_A)}{f_b(E_A)}\right]}{\frac{Q_f}{Q_m}\underbrace{n_i e^{\frac{\psi_s - V_{ch}}{U_T}}}_{\text{(a)}} - N_A\left(1 - \frac{U_T}{f_s(E_A)}\frac{\partial f_s(E_A)}{\partial\psi_s}\right)}\frac{\partial V_{GB}}{\partial\psi_s}. \tag{19}$$

The following relation can be derived for (a) in (19) (see the Appendix):

$$n_i e^{\frac{\psi_s - V_{ch}}{U_T}} = \frac{Q_m}{Q_f}\frac{2N_A\left[(\psi_s - \psi_b) - U_T \ln\frac{f_s(E_A)}{f_b(E_A)}\right]}{U_T}. \tag{20}$$

Plugging this in (19), one finds

$$\text{SS} = U_T \ln(10)\frac{1}{1 - \frac{U_T\left(1 - \frac{U_T}{f_s(E_A)}\frac{\partial f_s(E_A)}{\partial\psi_s}\right)}{2\left[(\psi_s - \psi_b) - U_T \ln\frac{f_s(E_A)}{f_b(E_A)}\right]}}\frac{\partial V_{GB}}{\partial\psi_s} \tag{21}$$

where

$$\frac{\partial V_{GB}}{\partial\psi_s} = 1 + \frac{\sqrt{2qN_A\varepsilon_{si}}}{C_{ox}}\frac{1 - \frac{U_T}{f_s(E_A)}\frac{\partial f_s(E_A)}{\partial\psi_s}}{2\sqrt{(\psi_s - \psi_b) - U_T \ln\frac{f_s(E_A)}{f_b(E_A)}}} - \frac{q}{C_{ox}}\sum_j N_{it,j}\frac{\partial f_s(E_{t,j})}{\partial\psi_s} \tag{22}$$

follows from the surface-boundary condition derived in Section III-B3. In the subthreshold region, far above the flat-band condition, $f_s(E_A) = 1$ can be assumed (Fig. 4), and $U_T \ll 2(\psi_s - \psi_b)$, leading to $\text{SS} = U_T \ln 10(\partial V_{GB}/\partial\psi_s)$ with

$$\frac{\partial V_{GB}}{\partial\psi_s} = 1 + \frac{\sqrt{2qN_A\varepsilon_{si}}}{C_{ox}}\frac{1}{2\sqrt{\psi_s - \psi_b}} - \frac{q}{C_{ox}}\sum_j N_{it,j}\frac{\partial f_s(E_{t,j})}{\partial\psi_s}. \tag{23}$$

Taking the derivative of (13), (23) becomes

$$\frac{\partial V_{GB}}{\partial\psi_s} = 1 + \frac{\sqrt{2qN_A\varepsilon_{si}}}{C_{ox}}\frac{1}{2\sqrt{\psi_s - \psi_b}} + \frac{q}{C_{ox}}\frac{1}{U_T}\sum_j N_{it,j}\frac{g_t \exp[(\psi_{t,j} - \psi_s)/U_T]}{\{1 + g_t \exp[(\psi_{t,j} - \psi_s)/U_T]\}^2}. \tag{24}$$

Note the appearance of a factor $1/U_T$ in the third term on the RHS of (24). Placing a discrete interface trap, $\psi_{t,j}$, at each ψ_s value in the subthreshold region, and assuming a uniform $N_{it,j}$ value for each trap, leads to

$$\frac{\partial V_{GB}}{\partial\psi_s} = 1 + \frac{\sqrt{2qN_A\varepsilon_{si}}}{C_{ox}}\frac{1}{2\sqrt{\psi_s - \psi_b}} + \frac{qN_{it}}{C_{ox}}\frac{1}{U_T}\frac{g_t}{(1 + g_t)^2}. \tag{25}$$

The first two terms in (25) yield the nonideality or slope factor without interface traps, n_0. The SS-expression becomes

$$\mathrm{SS} = n_0 U_T \ln 10 + \frac{q N_{\mathrm{it}}}{C_{\mathrm{ox}}} \frac{g_t}{(1+g_t)^2} \ln 10 \tag{26}$$

where the second term on the RHS is the sought Δ_{SS}-offset. The nonideality factor n_0 has an upper bound of two mainly related to doping. Therefore, at 4.2 K, the first term on the RHS of (26) is limited to ≈1.6 mV/decade. Note that N_{it} does not become multiplied with U_T in (26). Therefore, assuming a reasonable value for $N_{\mathrm{it}} = 3 \times 10^{11}$ cm^{-2}, the second term gives ≈9 mV/decade (with $C_{\mathrm{ox}} = 20$ mF m^{-2} and $g_t = 4$). Together they yield the SS-degradation observed on a long nMOS device at 4.2 K. At 77 K, a similar calculation using $n_0 = 1.08$ and $N_{\mathrm{it}} = 3 \times 10^{11}$ cm^{-2} gives 25 mV/decade, corresponding to the SS measured [31] on a long pMOS device at 77 K (Fig. 8).

VII. Conclusion

A theoretical MOS transistor model is developed valid from room temperature down to liquid-helium temperature. The model relies on the Boltzmann statistics, verified in the limit to 0 K, and includes incomplete ionization, interface traps, bandgap temperature dependence, and mobility reduction. It is evidenced that incomplete ionization maintains the nondegeneracy of a semiconductor at deep-cryogenic temperatures and leads to a decrease in the threshold voltage on top of the overall increase due to Fermi–Dirac distribution scaling. The Fermi–Dirac temperature dependence of interface-trap occupation degrades the SS down to 4.2 K. An expression for the SS, including incomplete ionization and temperature-dependent interface trapping, is derived. The proposed model builds the indispensable physical foundation for future low-temperature CMOS circuit design.

Appendix

Starting from $Q_m + Q_f = Q_{sc}$, we can write $(Q_m + Q_f)^2 = \varepsilon_{si}^2 \mathbf{E}_s^2$, with $\mathbf{E}_s$ given by (7). Solving a quadratic equation for Q_m leads to

$$\frac{Q_m}{Q_f} = -1 + \sqrt{1 + \frac{2 q n_i U_T \varepsilon_{si}}{Q_f^2} e^{\frac{\psi_s - V_{\mathrm{ch}}}{U_T}}} \tag{27}$$

where we neglected the exponential term in ψ_b / U_T. In the subthreshold region ($Q_m \ll Q_f$), $\sqrt{1+x}$ can be approximated by $1 + x/2$ for $x \to 0$. Using (11) for Q_f^2 leads to (20).

References

[1] F. Balestra and G. Ghibaudo, "Physics and performance of nanoscale semiconductor devices at cryogenic temperatures," *Semicond. Sci. Technol.*, vol. 32, no. 2, p. 023002, Jan. 2017.

[2] M. de Souza, V. Kilchtyska, D. Flandre, and M. A. Pavanello, "Liquid helium temperature analog operation of asymmetric self-cascode FD SOI MOSFETs," in *Proc. IEEE Int. Conf. SOI*, Oct. 2012, pp. 1–2.

[3] A. Beckers, F. Jazaeri, and C. Enz, "Characterization and modeling of 28 nm bulk CMOS technology down to 4.2 K" *IEEE J. Electron Devices Soc.*, Mar. 2018.

[4] C. G. Rogers, "MOST's at cryogenic temperatures," *Solid-State Electron.*, vol. 11, no. 11, pp. 1079–1091, 1968.

[5] R. K. Kirschman, "Cold electronics: An overview," *Cryogenics*, vol. 25, no. 3, pp. 115–122, 1985.

[6] E. A. Gutierrez-D, J. Deen, and C. Claeys, Eds., *Low Temperature Electronics: Physics, Devices, Circuits, and Applications*. New York, NY, USA: Academic, 2000.

[7] F. Balestra and G. Ghibaudo, *Device and Circuit Cryogenic Operation for Low Temperature Electronics*. New York, NY, USA: Springer, 2001.

[8] D. S. Holmes, A. L. Ripple, and M. A. Manheimer, "Energy-efficient superconducting computing—Power budgets and requirements," *IEEE Trans. Appl. Supercond.*, vol. 23, no. 3, Jun. 2013, Art. no. 1701610.

[9] F. A. Zwanenburg *et al.*, "Silicon quantum electronics," *Rev. Mod. Phys.*, vol. 85, pp. 961–1019, Jul. 2013.

[10] S. De Franceschi, L. Kouwenhoven, C. Schonenberger, and W. Wernsdorfer, "Hybrid superconductor–quantum dot devices," *Nature Nanotechnol.*, vol. 5, no. 10, pp. 703–711, Oct. 2010.

[11] J. J. Pla *et al.*, "A single-atom electron spin qubit in silicon," *Nature*, vol. 489, no. 7417, pp. 541–545, 2012.

[12] R. Maurand *et al.*, "A CMOS silicon spin qubit," *Nature Commun.*, vol. 7, Nov. 2016, Art. no. 13575.

[13] L. M. K. Vandersypen *et al.*, "Interfacing spin qubits in quantum dots and donors—Hot, dense, and coherent," *npj Quantum Inf.*, vol. 3, no. 1, Art. no. 34, Sep. 2017.

[14] S. R. Ekanayake, T. Lehmann, A. S. Dzurak, R. G. Clark, and A. Brawley, "Characterization of SOS-CMOS FETs at low temperatures for the design of integrated circuits for quantum bit control and readout," *IEEE Trans. Electron Devices*, vol. 57, no. 2, pp. 539–547, Feb. 2010.

[15] D. J. Reilly, "Engineering the quantum-classical interface of solid-state qubits," *npj Quantum Inf.*, vol. 1, p. 15011, Oct. 2015.

[16] M. Rahman and T. Lehmann, "A cryogenic DAC operating down to 4.2 K," *Cryogenics*, vol. 75, pp. 47–55, Apr. 2016.

[17] D. P. DiVincenzo. (2000). "The physical implementation of quantum computation." [Online]. Available: https://arxiv.org/abs/quant-ph/0002077

[18] M. A. Nielsen and I. L. Chuang, *Quantum Computation and Quantum Information*, 10th ed. Cambridge, U.K.: Cambridge Univ. Press, 2010.

[19] V. Revéret *et al.*, "CESAR: Cryogenic electronics for space applications," *J. Low Temp. Phys.*, vol. 176, nos. 3–4, pp. 446–452, 2014.

[20] P. Merken, T. Souverijns, J. Putzeys, Y. Creten, and C. V. Hoof, "Flight qualification and circuit development of sensor front-end electronics for PACS/Hershel at liquid helium temperature," *J. Microelectron. Electron. Packag.*, vol. 4, no. 4, pp. 130–135, 2007.

[21] J. R. Hoff, G. W. Deptuch, G. Wu, and P. Gui, "Cryogenic lifetime studies of 130 nm and 65 nm nMOS transistors for high-energy physics experiments," *IEEE Trans. Nucl. Sci.*, vol. 62, no. 3, pp. 1255–1261, Jun. 2015.

[22] B. Okcan, P. Merken, G. Gielen, and C. van Hoof, "A cryogenic analog to digital converter operating from 300 K down to 4.4 K," *Rev. Sci. Instrum.*, vol. 81, no. 2, p. 024702, Feb. 2010.

[23] F. R. Ihmig, S. G. Shirley, R. K. Kirschman, and H. Zimmermann, "Frozen cells and bits: Cryoelectronics advances biopreservation," *IEEE Pulse*, vol. 4, no. 5, pp. 35–43, Sep. 2013.

[24] P. Martin, M. Cavelier, R. Fascio, G. Ghibaudo, and M. Bucher, "EKV3 compact modeling of MOS transistors from a 0.18 μm CMOS technology for mixed analog/digital circuit design at low temperature," *Cryogenics*, vol. 49, no. 11, pp. 595–598, 2009.

[25] Y. Creten, P. Merken, W. Sansen, R. Mertens, and C. van Hoof, "A cryogenic ADC operating down to 4.2 K," in *IEEE Int. Solid-State Circuits Conf. (ISSCC) Dig. Tech. Papers*, Feb. 2007, pp. 468–616.

[26] Y. Tsividis and C. McAndrew, *Operation and Modeling of the MOS Transistor*. London, U.K.: Oxford Univ. Press, 2011.

[27] S. M. Sze and K. K. Ng, *Physics of Semiconductor Devices*. Hoboken, NJ, USA: Wiley, 2006.

[28] A. Akturk *et al.*, "Compact and distributed modeling of cryogenic bulk MOSFET operation," *IEEE Trans. Electron Devices*, vol. 57, no. 6, pp. 1334–1342, Jun. 2010.

[29] A. Akturk, J. Allnutt, Z. Dilli, N. Goldsman, and M. Peckerar, "Device modeling at cryogenic temperatures: Effects of incomplete ionization," *IEEE Trans. Electron Devices*, vol. 54, no. 11, pp. 2984–2990, Nov. 2007.

[30] A. Akturk *et al.*, "Compact modeling of 0.35 μm SOI CMOS technology node for 4 K DC operation using Verilog-A," *Microelectron. Eng.*, vol. 87, no. 12, pp. 2518–2524, 2010.

[31] A. Beckers, F. Jazaeri, A. Ruffino, C. Bruschini, A. Baschirotto, and C. Enz, "Cryogenic characterization of 28 nm bulk CMOS technology for quantum computing," in *Proc. 47th Eur. Solid-State Device Res. Conf. (ESSDERC)*, Sep. 2017, pp. 62–65.

[32] A. Beckers, F. Jazaeri, H. Bohuslavskyi, L. Hutin, S. D. Franceschi, and C. Enz, "Design-oriented modeling of 28 nm FDSOI CMOS technology down to 4.2 K for quantum computing," in *Proc. Joint Int. EUROSOI Workshop Int. Conf. Ultimate Integr. Silicon (EUROSOI-ULIS)*, Mar. 2018, pp. 1–4.
[33] I. M. Hafez, G. Ghibaudo, and F. Balestra, "Assessment of interface state density in silicon metal-oxide-semiconductor transistors at room, liquid-nitrogen, and liquid-helium temperatures," *J. Appl. Phys.*, vol. 67, no. 4, pp. 1950–1952, Feb. 1990.
[34] A. K. Jonscher, "Semiconductors at cryogenic temperatures," *Proc. IEEE*, vol. 52, no. 10, pp. 1092–1104, Oct. 1964.
[35] D. P. Foty, "Impurity ionization in MOSFETs at very low temperatures," *Cryogenics*, vol. 30, no. 12, pp. 1056–1063, 1990.
[36] R. C. Jaeger and F. H. Gaensslen, "Simulation of impurity freezeout through numerical solution of Poisson's equation with application to MOS device behavior," *IEEE Trans. Electron Devices*, vol. ED-27, no. 5, pp. 914–920, May 1980.
[37] M. Turowski and A. Raman, "Device-circuit models for extreme environment space electronics," in *Proc. 19th Int. Conf. Mixed Design Integr. Circuits Syst. (MIXDES)*, May 2012, pp. 350–355.
[38] M. Kantner and T. Koprucki, "Numerical simulation of carrier transport in semiconductor devices at cryogenic temperatures," *Opt. Quantum Electron.*, vol. 48, no. 12, p. 543, 2016.
[39] R. F. Pierret and G. W. Neudeck, *Advanced Semiconductor Fundamentals*, vol. 6. Reading, MA, USA: Addison-Wesley, 1987.
[40] S. H. Wu and R. L. Anderson, "MOSFET's in the 0 K approximation: Static characteristics of MOSFET's in the 0 K approximation," *Solid-State Electron.*, vol. 17, no. 11, pp. 1125–1137, 1974.
[41] K. A. Wilson, P. L. Tuxbury, and R. L. Anderson, "A simple analytical model for the electrical characteristics of depletion-mode MOSFET's with application to low-temperature operation," *IEEE Trans. Electron Devices*, vol. ED-33, no. 11, pp. 1731–1737, Nov. 1986.
[42] J.-J. Sim and J. B. Kuo, "An analytical delayed-turn-off model for buried-channel PMOS devices operating at 77 K," *IEEE Trans. Electron Devices*, vol. 39, no. 4, pp. 939–947, Apr. 1992.
[43] I. M. Hafez, F. Balestra, and G. Ghibaudo, "Characterization and modeling of silicon metal-oxide-semiconductor transistors at liquid-helium temperature: Influence of source-drain series resistances," *J. Appl. Phys.*, vol. 68, no. 7, pp. 3694–3700, 1990.
[44] Y. P. Varshni, "Temperature dependence of the energy gap in semiconductors," *Physica*, vol. 34, no. 1, pp. 149–154, 1967.
[45] P. Altermatt, A. Schenk, and G. Heiser, "A simulation model for the density of states and for incomplete ionization in crystalline silicon. II. Investigation of Si:As and Si:B and usage in device simulation," *J. Appl. Phys.*, vol. 100, no. 11, p. 113715, 2006.
[46] F. Jazaeri, C.-M. Zhang, A. Pezzotta, and C. Enz, "Charge-based modeling of radiation damage in symmetric double-gate MOSFETs," *IEEE J. Electron Devices Soc.*, vol. 6, no. 1, pp. 85–94, Dec. 2018.
[47] F. Jazaeri and J.-M. Sallese, *Modeling Nanowire and Double-Gate Junctionless Field-Effect Transistors*. Cambridge, U.K.: Cambridge Univ. Press, 2018.
[48] A. Yesayan, F. Jazaeri, and J. M. Sallese, "Charge-based modeling of double-gate and nanowire junctionless FETs including interface-trapped charges," *IEEE Trans. Electron Devices*, vol. 63, no. 3, pp. 1368–1374, Mar. 2016.
[49] J.-M. Sallese, M. Bucher, F. Krummenacher, and P. Fazan, "Inversion charge linearization in MOSFET modeling and rigorous derivation of the EKV compact model," *Solid-State Electron.*, vol. 47, no. 4, pp. 677–683, 2003.
[50] G. Ghibaudo, "New method for the extraction of MOSFET parameters," *Electron. Lett.*, vol. 24, no. 9, pp. 543–545, Apr. 1988.
[51] S. K. Tewksbury, "Attojoule MOSFET logic devices using low voltage swings and low temperature," *Solid-State Electron.*, vol. 28, no. 3, pp. 255–276, 1985.
[52] R. Trevisoli, M. de Souza, R. T. Doria, V. Kilchtyska, D. Flandre, and M. A. Pavanello, "Junctionless nanowire transistors operation at temperatures down to 4.2 K," *Semicond. Sci. Technol.*, vol. 31, no. 11, p. 114001, Nov. 2016.

Arnout Beckers received the M.Sc. degree in nanoelectronics from KU Leuven, Leuven, Belgium, in 2016, carrying out his M.Sc. thesis at the Physics Modeling and Simulation Group, imec, Leuven.

He is currently a Doctoral Assistant with the Integrated Circuits Laboratory, École Polytechnique Fédérale de Lausanne, Lausanne, Switzerland, where he is involved in the research on cryogenic CMOS modeling. His current research interests include solid-state physics, low-temperature electronics, and quantum computing.

Farzan Jazaeri received the Ph.D. degree in microelectronics and microsystems from the École Polytechnique Fédérale de Lausanne (EPFL), Lausanne, Switzerland, in 2015.

He then joined the Integrated Circuits Laboratory, EPFL, as a Research Scientist and the Project Leader. His current research interests include solid-state physics and advanced semiconductor devices for operation within extreme harsh environments, i.e., high-energy particle background and cryogenic temperatures for space-based applications and quantum computations.

Christian Enz (M'84–SM'12) received the M.S. and Ph.D. degrees in electrical engineering from the École Polytechnique Fédérale de Lausanne (EPFL), Lausanne, Switzerland, in 1984 and 1989, respectively.

In 2013, he joined EPFL as a Full Professor, where he is currently the Director of the Institute of Microengineering and also the Head of the Integrated Circuits Laboratory. His technical interests and expertise are in the fields of very low-power analog and RF IC design and semiconductor device modeling.